



ELSEVIER

Ultramicroscopy 90 (2002) 85–95

ultramicroscopy

www.elsevier.com/locate/ultramicroscopy

# Reconstruction of the electric charge density in thin films from the contrast transfer function measurements

Krassimir Danov<sup>1</sup>, Radostin Danev, Kuniaki Nagayama\*

*National Institute for Physiological Sciences, Okazaki National Research Institutes, Myodaiji-cho, Okazaki 444-8585, Japan*

Received 14 August 2001; received in revised form 20 August 2001

## Abstract

The radial distribution of the beam-induced charge in thin films is investigated using the contrast transfer properties of the transmission electron microscope. The phase shift due to charging is measured as the phase difference between the contrast transfer functions of two photos taken with and without film at the back focal plane. Solving the inverse Laplace problem with this input data recovers the charge density of the measured film. The electric potential function in the whole area is reconstructed using the boundary integral method and the analytical solution of the Laplace equation for the electric potential is induced from unit step-wise surface charge. The phase shift of electron waves is derived in a weak lens approximation. In this way, the radial dependence of the charge density and the magnitude of the electrostatic potential at the thin film are obtained. The surface charge density reaches quasi-equilibrium state after the first 30 min of the electron beam pre-irradiation. The hydrocarbon contamination layer on the surface of the film is considered to be the main source of charging. An explanation of the qualitative behavior of the charge density, based on the contamination diffusion theory, is proposed. © 2002 Elsevier Science B.V. All rights reserved.

*PACS:* 61.16.Bg; 41.20.Cv

*Keywords:* Electric charge density; Phase shift; Electrostatic potential; Contrast transfer function

## 1. Introduction

The electron beam induced charging in thin material films is a well-known phenomenon [1]. The problem, related to scanning electron microscopy (SEM), is discussed in Ref. [2] and the different conditions in the transmission electron

microscope (TEM) are the subject of investigation in Ref. [3]. Non-conductive materials under high-energy electron bombardment are usually positively charged. This is due to the absence of conduction electrons to compensate for the emitted secondary and Auger electrons with yield higher than unity (i.e. for each trapped incident electron more than one is emitted). The trapped charge electrostatically interacts with the observation beam and in most cases has negative effect on the system performance.

Charging of non-conductive specimens may result in image deterioration [4] as well as specimen

\*Corresponding author. Tel: +81-564-55-7811; fax: +81-564-52-7913.

*E-mail address:* nagayama@nips.ac.jp (K. Nagayama).

<sup>1</sup>On temporary leave from the Laboratory of Chemical Physics Engineering, Sofia University, 1 J. Bourchier Avenue, 1164 Sofia, Bulgaria.

damage [3]. Conductive surfaces, which are subject to electron bombardment inside the electron-optical system (specimen support film, apertures, phase plates, sample holder, etc.), may be covered by non-conductive contaminants [5–9]. This can also give rise to charging which in turn degrades the system performance.

One application, where electron-induced charging is employed, is the electrostatic phase plate proposed by Unwin [10], where the potential distribution produced by charging of the central portion of thin thread is used as electrostatic lens. Recently, based on the idea of complex observation [11] for improvement of images, application of the Zernike phase plate to the TEM was reported [12]. The authors conclude that the major practical problem in such application is the electrostatic charging of the phase plate.

There are numerous experimental works utilizing electron holography in which the charging of dielectric spheres, as well as electric potentials and magnetic fields in solids, have been investigated [13–16]. Innovative approach is used in Ref. [4] for the investigation on the charging of biological cryo-samples. The change of the beam diameter and defocused diffraction observation after irradiation of a small area are used for quantification of the charge magnitude.

A new experimental technique for the measurement of the electron wave phase shift due to charging is described in Ref. [17]. Using the fact that the electron waves traveling through electrostatic field experience phase shift, the method exploits the phase contrast transfer properties of the TEM.

The theoretical modeling of the phase shift of electron waves is based on the numerical solution of the Laplace equation for the electric potential using various geometries of walls and boundary conditions for the electric potential at them [1,2,18,19]. Matsumoto and Tonomura [20] proved from the solution of the Laplace equation that the phase shift, which is proportional to the potential integrated along the optical axis, is constant inside the ring of a Boersch phase plate. For the case of charging effects in thin film phase plates and thin foil lenses, the problem of electron phase shift determination is solved in Ref. [17]. The influence

of the geometry of the aperture and the size of the central hole in the case of Zernike phase plate is taken into account in a recent work [21]. Similar problems appear when a foil lens is applied after the objective lens of a conventional TEM for reduction of the spherical aberration [22,23].

All these theoretical works do not give an idea about the solution of the inverse Laplace problem, which is important for the reconstruction of the physical parameters from experimental data. From a mathematical viewpoint, the solution of the inverse Laplace problem is much easier if the boundary conditions for the potential at the surfaces are postulated. Then for example, the surface potential at the irradiated film can be reconstructed. Unfortunately, this solution will not be a great success because in order to find the surface charge, the second derivative from the reconstructed data has to be taken. It is a well-known fact that the error in the second derivative of experimental curves is very large and some times it is not possible to extract any information. Therefore, the inverse Laplace problem has to be solved for the direct reconstruction of the surface charge distribution.

The article is outlined as follows. In Section 2, the experimental results for the phase difference between the contrast transfer functions (CTFs) of two photos taken with and without film at the back focal plane are described. The measured normalized electron beam intensity gives additional information about the geometry of the charging area. The solution of the inverse Laplace problem for the reconstruction of the electric charge density is developed in Section 3. The phase shift of electron waves is derived in a weak lens approximation. With this method, the radial dependence of the charge density and the magnitude of the electrostatic potential at the thin film are obtained in Section 4. Finally, in Section 5 we draw some conclusions.

## 2. Experimental data

A sketch of the investigated system is shown in Fig. 1. Thin material film is supported on an aperture with radius  $r_a$  situated at the back-focal

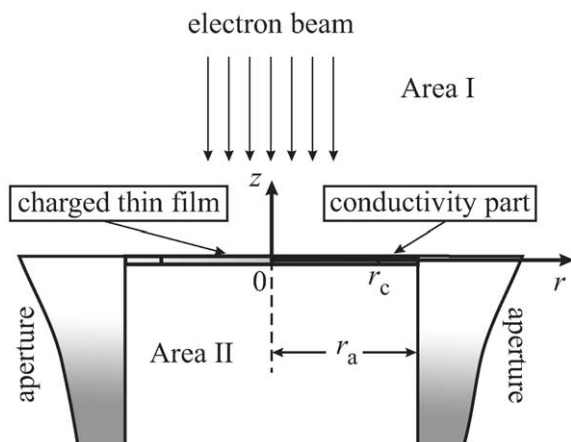


Fig. 1. A sketch of the investigated system.

plane of the objective lens. The aperture is centered relative to the optical axis so that the main beam illuminates a small area around the center of the film. The size of the illuminated area can be varied by shifting the aperture along the optical axis (the  $z$ -axis in Fig. 1) thus changing the focus of the zero-diffraction spot on the film. Due to the electron irradiation, the film is charged forming a three-dimensional electrostatic potential distribution in the surrounding space. The potential is assumed to be zero at the aperture surfaces. The surface potential of the film in the ring area between  $r_c$  and  $r_a$  is considered to be zero too (see the explanation in Ref. [17]). The electrostatic field causes a phase shift to the electron waves, which combined with the one due to defocus and spherical aberration determines the CTF of the microscope. In order to measure only the phase shift due to charging, two photos are taken at the same defocus—one with film and one without film at the back-focal plane. The phase shift due to defocus and spherical aberration is determined from the CTF in the second photo. Then it is subtracted from the phase shift in the CTF of the first photo thus leaving only the one due to charging. The detailed description of the procedure is given in Ref. [17].

The extraction of the phase shift due to charging is illustrated in Fig. 2. The phase shift from each photo is extracted by fitting the positions of the

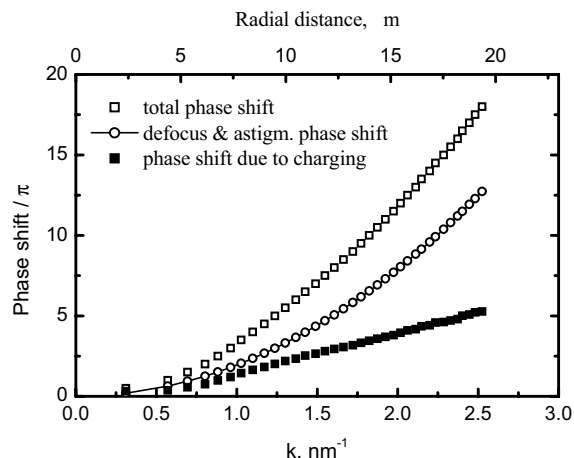


Fig. 2. Illustration of the phase shift due to charging extraction. The total phase shift is from the CTF of a photo taken with material film at the back-focal plane. The phase shift due to defocus and spherical aberration is from a photo taken without film at the back-focal plane. The difference between the two phase shifts gives the phase shift due to charging.

extrema in the rotationally averaged CTF profile. The phase step between two adjacent extrema (minimum and maximum) is  $\pi/2$ . In our experiments, the material film is usually charged positively due to the emission of secondary electrons exceeding the amount of the captured. This gives effect similar to overfocusing because the central portion of the electron wave at the back-focal plane retards relatively to the outer part. Taking the photos at overfocus condition (defocus  $< 0$ ) gives the advantage of easier processing of the data. In this case, the phase shift in the CTFs is positive and it increases monotonously.

For our experiments, we used JEOL JEM-4010N transmission electron microscope with LaB<sub>6</sub> gun operated at 300 kV ( $C_S = 3$  mm). Amorphous carbon film with thickness  $32 \pm 1$  nm was prepared by vacuum evaporation on freshly cleaved mica, floated on water and transferred on standard 50  $\mu\text{m}$  molybdenum apertures. The apertures were then placed in the objective lens aperture holder and inserted into the microscope. The aperture holder was positioned slightly below the back-focal plane giving more spread

central beam on the film. In order to reduce the effects of contamination, we used the microscope's built-in anti-contamination device in all experiments.

In our trial experiments, we observed a change in the charging properties of the film due to the irradiation of the film by the electron beam. In the literature, the characteristic time for the charge to reach equilibrium is given in the order of several seconds [1]. We could not observe this initial charge buildup as it is too fast for our experimental technique. However, a decrease in the change magnitude was observed after the film was irradiated for minutes. In order to investigate this effect, three measurements of the phase shift due to the charging were performed—without pre-irradiation, after 30 min of pre-irradiation, and after 30 more minutes or a total of 60 min of pre-irradiation. Each measurement consisted of four photos: two defocus values and two photos at each defocus—one with film and one without film at the back-focal plane. Combining the data from several defocuses increases the number of data points thus improving the statistics. The pre-irradiation was performed by spreading of the electron beam so that the whole aperture opening to be covered by the beam. Pre-irradiation of 30 min gives a total dose of around  $2000 \text{ e}^-/\text{nm}^2$  to the film. After each pre-irradiation, the aperture is retracted and left for 5 min outside the beam. This procedure is used for temperature stabilization and relaxation of short-time processes before the photos are taken. The photographic exposure was 2 s with a beam current of around  $6 \times 10^{-9} \text{ A}$  (measured with the microscope's built-in electrometer).

The charge distribution of the measured film is expected to correlate with the radial dependence of the electron beam intensity. Hence, we pay a special attention for the measurement of the beam intensity distribution. The beam profile at the film was measured in diffraction mode by focusing on the aperture and taking a snapshot with an inline  $2\text{K} \times 2\text{K}$  CCD camera. The CCD camera was not used for the phase shift measurement as it offers much lower total pixel number compared to the photographic film (i.e. lower signal-to-noise ratio in the CTF data).

The results for the phase shifts from the three measurements are given in Fig. 3. In each figure, the measured beam profile normalized through its maximum intensity is also plotted. The illustrated phase shift dataset is a combination of measurements at two defocuses—open and filled symbols. The corresponding values of the defocuses are given in the legends of Figs. 3a–c. It is seen from Figs. 3a–c that the difference between the experimental points, obtained at the two defocuses, is small. The dashed line in Figs. 3a–c represents the best polynomial fit for each dataset. We used only polynomials of even powers of the radial distance. This requirement comes from the symmetry of the Laplace problem in cylindrical coordinates (see Section 4 for details about the data processing). The final conclusion from the experimental data is that: the first pre-irradiation (30 min) reduces the phase shift due to charging about 2 times (compare Figs. 3a and b); further irradiation has no significant effect on the phase shift (compare Figs. 3b and c).

The phase shift measurements give some quantitative information about the magnitude of the total charge trapped in the specimen. The larger the phase shift due to charging the larger the total charge in the specimen. Moreover, the radial dependence of the measured phase shift contains information about the radial distribution of this charge. To extract this information, the inverse Laplace problem has to be solved.

### 3. Theoretical model for the reconstruction of the film charge density

In order to reconstruct the film charge density  $\rho$  from the experimental data, presented in Section 2, the inverse Laplace problem for the electric potential function is solved. We will consider the case of axial symmetry and thin films when  $\rho$  depends only on the radial coordinate  $r$ . The electrostatic potential function at the phase plate  $U$  is a solution of the one-dimensional Poisson equation [1]

$$\frac{1}{r} \frac{d}{dr} \left( r \frac{dU}{dr} \right) = -\frac{\rho}{\epsilon_0 \epsilon_r} \quad \text{for } 0 \leq r \leq r_c, \quad (1)$$

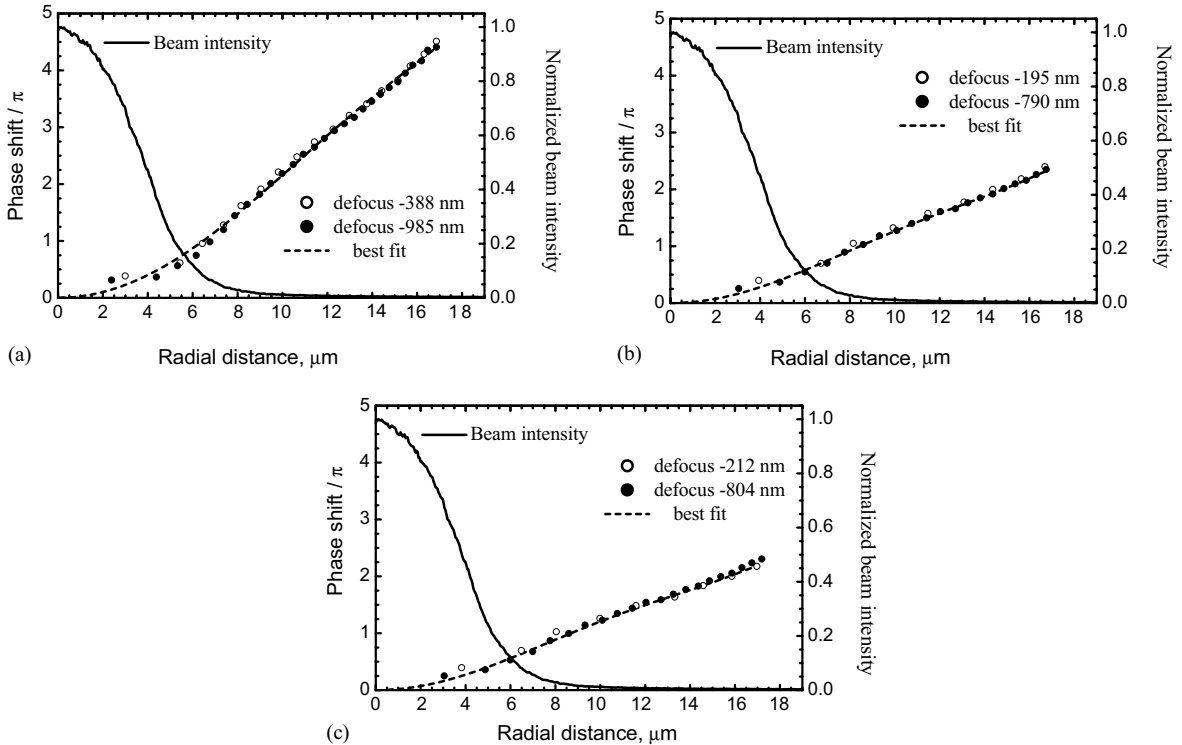


Fig. 3. Experimental data for the measured phase shift due to charging after different pre-irradiation times: (a) without pre-irradiation; (b) after 30 min of pre-irradiation; and (c) after 60 min of pre-irradiation. The solid line is the beam intensity profile. The dashed lines are the best polynomial approximations of the data.

where  $\epsilon_0$  is the dielectric constant,  $\epsilon_r$  is the relative dielectric permittivity of the film and  $r_c$  is the radius of the boundary between the conductive and charged film parts. Generally,  $r_c$  should be equal to the radius of the aperture  $r_a$ , but the experimental results reported in Ref. [17] show that in some cases  $r_c < r_a$ . In such cases, the charging occurs mainly at the surface of the film where some contamination could reside. Then the film is assumed to be conducting and the contamination layer acts as an insulating covering.

We will consider the spatial dependence of the electrostatic potential function,  $V(r, z)$ , in the case of axial symmetry, where the vertical axis  $Oz$  of the cylindrical coordinate system coincides with the axis of symmetry and the film coincides with the zero plane,  $z = 0$  (see Fig. 1). The film separates the calculation area into two parts. The semi-infinite region above the aperture, called here as

“area I”, is described by  $z \geq 0$ . The region below the film is a cylinder with radius  $r_a$  and depth  $d_a$ , given by  $0 \leq r \leq r_a$  and  $-d_a \leq z \leq 0$ , called “area II”. The typical apertures used in the TEM have depths more than 2 times larger than diameters. Therefore, the assumption that the phase shift of the electron wave does not depend on the aperture depth can be applied. In the case of axial symmetry, the electrostatic potential function  $V$  is a solution of the two-dimensional Laplace equation [2]

$$\frac{1}{r} \frac{\partial}{\partial r} \left( r \frac{\partial V}{\partial r} \right) + \frac{\partial^2 V}{\partial z^2} = 0 \quad (2)$$

in the working areas I and II. The partial differential Eq. (2) is solved using Eq. (1) and the boundary conditions that at the aperture wall the electrostatic potential function is zero and it vanishes at infinity.

Knowing the electric potential in the whole region, the phase shift  $\varphi$  of the electron wave due to the charging of the film can be estimated in a weak lens approximation [17,20,21] as

$$\varphi(r) = -\pi \frac{1 + 2\alpha U_0}{1 + \alpha U_0} \frac{1}{\lambda U_0} \int_{-\infty}^{\infty} V(r, z) dz + \varphi_f(r), \quad (3)$$

where  $\lambda$  is the electron wavelength,  $U_0$  is the accelerating voltage, and  $\alpha = 0.9785 \times 10^{-6} \text{ V}^{-1}$ . In Eq. (3),  $\varphi_f(r)$  is the phase shift of the electron wave corresponding to the internal potential  $V_{\text{in}}$  and the surface potential  $U(r)$ .  $\varphi_f(r)$  is calculated using the simple formula

$$\varphi_f(r) = -\pi \frac{1 + 2\alpha U_0}{1 + \alpha U_0} \frac{h}{\lambda U_0} [U(r) + V_{\text{in}}]. \quad (4)$$

The internal potential  $V_{\text{in}}$  is an intrinsic property of the specimen material. As it was shown in the literature [17,21] for thin films, the phase shift calculated from the electrostatic potential in the working area is 2 orders of magnitude larger than the part of  $\varphi_f$  corresponding to the surface potential  $U$ . (The typical thickness of the film is  $h \approx 30 \text{ nm}$  and the radius of the electron beam is in the range  $5\text{--}10 \mu\text{m}$ .) Therefore, the integral in Eq. (3) should give the radial dependence of  $\varphi$ , shown in Fig. 3.

Problems (1)–(3) have no analytical solution and the classical numerical methods are also not applicable [24]. For that reason we will use the idea of the boundary integral method [24]. Following this idea, the interval  $[0, r_c]$  is divided into  $N$  subintervals by points  $r_0 \equiv 0, r_1, \dots, r_N \equiv r_c$ . The unknown charge density function  $\rho$  divided by the relative permittivity  $\varepsilon_r$  is represented as a sum of unit step-wise model functions (see Fig. 4) with amplitudes  $\rho_k \equiv \rho(r_k)/\varepsilon_r(r_k)$ ,  $k = 1, 2, \dots, N$ . Then the surface potential function  $U_k$  which corresponds to the  $k$ -step-wise charge function is a solution of the one-dimensional Eq. (1). The final results for  $U_1(r)$  read as

$$\begin{aligned} \frac{4\varepsilon_0 U_1}{\rho_1 r_1^2} &= 1 + 2 \ln\left(\frac{r_c}{r_1}\right) - \frac{r^2}{r_1^2} \quad \text{for } 0 \leq r \leq r_1, \\ \frac{2\varepsilon_0 U_1}{\rho_1 r_1^2} &= \ln\left(\frac{r_c}{r}\right) \quad \text{for } r_1 \leq r \leq r_c; \end{aligned} \quad (5)$$

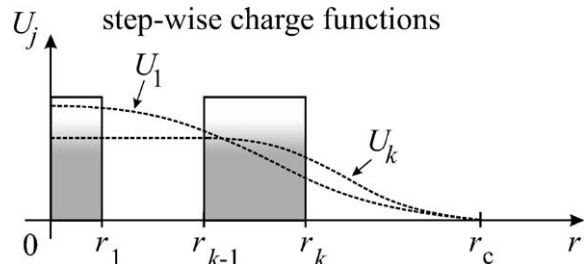


Fig. 4. Illustration of the step-wise charge density approach. For each charge step function, the surface potential is calculated and then used as boundary condition for the Laplace problem.

and for all other surface potential functions  $U_k(r)$  ( $k = 2, 3, \dots, N$ )

$$\begin{aligned} &\frac{4\varepsilon_0 U_k}{\rho_k (r_k^2 - r_{k-1}^2)} \\ &= 1 + \frac{2r_k^2}{r_k^2 - r_{k-1}^2} \ln\left(\frac{r_c}{r_k}\right) + \frac{2r_{k-1}^2}{r_k^2 - r_{k-1}^2} \ln\left(\frac{r_{k-1}}{r_c}\right) \end{aligned}$$

for  $0 \leq r \leq r_{k-1}$ ,

$$\begin{aligned} &\frac{4\varepsilon_0 U_k}{\rho_k (r_k^2 - r_{k-1}^2)} \\ &= \frac{r_k^2 - r^2}{r_k^2 - r_{k-1}^2} + \frac{2r_k^2}{r_k^2 - r_{k-1}^2} \ln\left(\frac{r_c}{r_k}\right) \\ &\quad + \frac{2r_{k-1}^2}{r_k^2 - r_{k-1}^2} \ln\left(\frac{r}{r_c}\right) \quad \text{for } r_{k-1} \leq r \leq r_k, \end{aligned}$$

$$\frac{2\varepsilon_0 U_k}{\rho_k (r_k^2 - r_{k-1}^2)} = \ln\left(\frac{r_c}{r}\right) \quad \text{for } r_k \leq r \leq r_c. \quad (6)$$

Because of the linearity of the Laplace equation (2), the solution of the problem for the electric potential function can be presented as a superposition of the simpler problems, corresponding to each step-wise charge function. This model gives a very high efficiency of the numerical computations only when the simpler problem has an analytical solution [24]. Otherwise, the numerical method is equivalent to the classical difference methods. Fortunately, the particular Laplace problems have simple solutions. For the first surface

potential function,  $U_1(r)$ , the corresponding space dependence of the electric potential function  $V_1(r, z)$  and the corresponding radial dependence of the phase shift  $\varphi_1(r)$  are reported in Ref. [17].

The analytical solution of the Laplace equation in the areas I and II are different because of the different boundary conditions at the aperture wall. In area I, the general solution of Eq. (2) is presented, applying the Fourier–Bessel integral transformation [2], as

$$V_k = \frac{\rho_k(r_k^2 - r_{k-1}^2)}{4\epsilon_0} \times \int_0^\infty \tilde{U}_k(s) \exp\left(-s \frac{z}{r_c}\right) J_0\left(s \frac{r}{r_c}\right) s \, ds, \quad (7)$$

where  $J_n$  is the Bessel function of the  $n$ th order,  $\tilde{U}_k(s)$  is the Fourier–Bessel transform of the dimensionless electrostatic potential function at the zero plane, and  $V_k(r, z)$  is the electrostatic potential function corresponding to the  $k$ -step-wise charge distribution. The negative sign in the exponent of solution (7) is used in order to satisfy the boundary condition at infinity, i.e. the electrostatic potential function is assumed to be zero at  $z \rightarrow \infty$ . If the boundary condition (6) is substituted into the general solution (7) and the inverse Fourier–Bessel transformation is taken, then the analytical result for the image  $\tilde{U}_k(s)$  can be calculated. Using the similar mathematical procedure as in Refs. [17,21], the final result can be written in the following form

$$\tilde{U}_k(s) = \frac{2}{s^2} \left\{ \frac{r_k^2}{r_k^2 - r_{k-1}^2} \left[ J_2\left(s \frac{r_k}{r_c}\right) + J_0\left(s \frac{r_k}{r_c}\right) \right] - \frac{r_{k-1}^2}{r_k^2 - r_{k-1}^2} \left[ J_2\left(s \frac{r_{k-1}}{r_c}\right) + J_0\left(s \frac{r_{k-1}}{r_c}\right) \right] - J_0(s) \right\} \quad (8)$$

for  $k = 1, 2, \dots, N$ . For  $k = 1$ ,  $r_0 = 0$ , and  $r_1 = a$ , where  $a$  is the measure of the electron beam radius used in Ref. [17], formula (8) gives the respective result for the Fourier–Bessel image from Ref. [17].

In area II, the general solution of the Laplace equation (2) for the electrostatic potential

function  $V_k(r, z)$  is presented as a Fourier–Bessel series [2]

$$V_k = \frac{\rho_k(r_k^2 - r_{k-1}^2)}{4\epsilon_0} \sum_{i=1}^\infty A_{ki} \exp\left(\alpha_i \frac{z}{r_a}\right) J_0\left(\alpha_i \frac{r}{r_a}\right), \quad (9)$$

where  $\alpha_i$  is the  $i$ th zero of the Bessel function  $J_0$ , i.e.  $J_0(\alpha_i) = 0$  and  $A_{ki}$  are constants, which are determined from the boundary condition at the film surface. This form of the solution obeys the boundary conditions at the aperture wall and at infinity (see Ref. [17]). For the constants  $A_{ki}$  after the substitution of Eq. (6) into Eq. (9) and taking into account the orthogonality of the Bessel functions with respect to their zeros, the following relationship is derived

$$A_{ki} = \frac{4}{\alpha_i^2 J_1^2(\alpha_i)} \times \left\{ \frac{r_k^2}{r_k^2 - r_{k-1}^2} \left[ J_2\left(\alpha_i \frac{r_k}{r_a}\right) + J_0\left(\alpha_i \frac{r_k}{r_a}\right) \right] - \frac{r_{k-1}^2}{r_k^2 - r_{k-1}^2} \left[ J_2\left(\alpha_i \frac{r_{k-1}}{r_a}\right) + J_0\left(\alpha_i \frac{r_{k-1}}{r_a}\right) \right] - J_0\left(\alpha_i \frac{r_c}{r_a}\right) \right\}, \quad (10)$$

for  $k = 1, 2, \dots, N$  and  $i = 1, 2, \dots$ . For  $k = 1$ ,  $r_0 = 0$ , and  $r_1 = a$ , formula (10) gives the respective result for the coefficients of the Fourier–Bessel series from Ref. [17].

Because of the linearity of the problem, the main part of the phase shift of electron waves due to the charging of the film can be presented as a superposition of the phase shifts  $\varphi_k$  corresponding to each  $k$ -step-wise charge distribution. Therefore,  $\varphi = \varphi_1 + \dots + \varphi_N$ ,

$$\varphi_k(r) = -\pi \frac{1 + 2\alpha U_0}{1 + \alpha U_0} \frac{1}{\lambda U_0} \int_{-\infty}^\infty V_k(r, z) \, dz. \quad (11)$$

If the general solutions (7) and (9) are substituted into Eq. (11), the phase shift function  $\varphi_k$  can be calculated as

$$\varphi_k(r) = \pi \frac{1 + 2\alpha U_0}{1 + \alpha U_0} \frac{r_a(r_k^2 - r_{k-1}^2)}{2\lambda U_0} (f_{I,k} + f_{II,k}) \rho_k, \quad (12)$$

where the dimensionless phase shift factors of areas I and II are  $f_{I,k}$  and  $f_{II,k}$ , respectively. The phase shift factors are calculated from the relationships

$$f_{I,k} = -\frac{r_c}{2r_a} \int_0^\infty \tilde{U}_k(s) J_0\left(s \frac{r}{r_c}\right) s ds,$$

$$f_{II,k} = -\frac{1}{2} \sum_{i=1}^{\infty} \frac{A_{ki}}{\alpha_i} J_0\left(\alpha_i \frac{r}{r_a}\right). \quad (13)$$

The integral, appearing in Eq. (13) has an analytical form, which is more convenient for the numerical calculations than the integral representation (see Appendix A).

The function multiplying  $\rho_k$  in Eq. (12) corresponds to the unit charge step-wise distribution and they are universal for the problem. Therefore, if we know the experimental data for the phase shift (see Fig. 3), the inverse Laplace problem is transformed to a simple linear optimization procedure for the amplitudes  $\rho_k$ .

#### 4. Results and discussions

Our numerical investigation shows that even six intervals of the charge density are enough to achieve good agreement between the experimental points and the theoretical phase shift function. The numerical results for the phase shift function in the case of Fig. 3a and six charge intervals are plotted in Fig. 5a. Therein, the best polynomial fit of the experimental data is also drawn. The difference between them is very small and practically both curves coincide. The corresponding charge density step-wise functions are illustrated in Fig. 5b (bar graph). Further increase of the number of intervals  $N$  leads only to the appearance of false oscillations in the final results because the procedure assumes precise input data. In order to find a smooth charge density distribution, one can interpolate the found six steps (Fig. 5b). This way is not preferable because we do not have any prior knowledge of the behavior of the charge density. The other variant to receive a smooth charge density distribution is to approximate the original experimental data with a smooth curve. Then substitut-

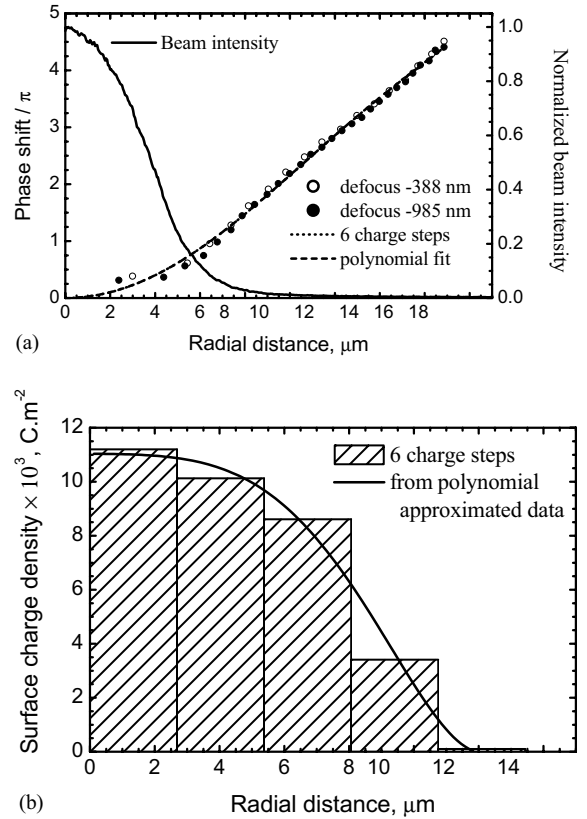


Fig. 5. Comparison between the two approaches: fitting of the original experimental data with few charge steps and fitting of polynomial approximated experimental data with a lot of charge steps. (a) The result of the six-step calculation for the charging phase shift coincides with the polynomial approximation curve. (b) Radial charge density distributions. Both results are practically the same with the polynomial approximation method providing much smoother results (more points).

ing this curve (shown in Fig. 3a) as input data we recover the charge density distribution represented by a large number of intervals. The resulting charge density function is plotted in Fig. 5b (solid line). It is well illustrated that the solid line follows the results from the six charge-step reconstruction. From our viewpoint, interpolation of the original data is more physical because the decision about the quality of the approximation in the experimental data space is easier. It is important to know that in the case of axial symmetry, the solutions depend on  $r^2$  and the interpolation of the

experimental data has to be done also as a function of  $r^2$ . In all cases calculated below, we compared the results from both approaches and found a good agreement between them (similar to that shown in Fig. 5).

The calculated distributions of the electric potential at the zero plane are plotted in Fig. 6a. The different style of lines corresponds to the experimental data for different pre-irradiation times (see Figs. 3a–c). The calculated radius at which the surface potential becomes zero is about  $19\ \mu\text{m}$  in all cases. The surface potential is positive which means that the irradiated film is positively charged. The magnitude of the surface potential at the center of the film is very low, about  $100\ \text{mV}$ . It drops down with increasing of the radial distance for all experiments. The surface potential changes significantly after the first 30 min

of the pre-irradiation. Its maximum in the center of the electron beam decreases from  $176$  to  $101\ \text{mV}$ . Pre-irradiating the film for 30 more minutes (or total of  $60\ \text{min}$ ) results in a much smaller change of the surface potential maximum (it drops to  $92.6\ \text{mV}$ ). This indicates that the system approaches equilibrium and further pre-irradiation will not significantly influence the surface potential. Rough estimation of the potential due to DC resistivity of the material using the following parameters:  $20\%$  inelastic scattering (see Ref. [12]),  $4.0$  emitted electrons per inelastic event,  $1.64 \times 10^{-5}\ \Omega\text{m}$  specific resistivity (bulk graphite); gives  $0.7\ \mu\text{V}$  in the center of the film. The measured potential of about  $100\ \text{mV}$  after pre-irradiation is about 5 orders higher in magnitude. Such a big difference cannot be explained by reduced conductivity of the film due to its thinness. Here, we can draw the conclusion that the main origin of the charging is the contamination layer on the surface of the film. It is important to note that the shape of the curves for the surface potential is similar to the one for the phase shift. Therefore, the surface potential distribution is not giving much more information about the charging effect.

The reconstructed charge density,  $\rho_k \equiv \rho(r_k)/\epsilon_r(r_k)$ , distributions from the experimental data are plotted in Fig. 6b. For better illustration of the correlation between the charge density distribution and the electron beam intensity, the measured normalized intensity is also given in Fig. 6b. It should be noted that the material properties of the film and the real charge density are not known. They both can vary as a function of the electron beam intensity and the time of pre-irradiation. Therefore, we can make quantitative conclusions only for the ratio  $\rho_k \equiv \rho(r_k)/\epsilon_r(r_k)$ , which we call “charge density”. The radial distributions of the charge density without pre-irradiation and after 30 and/or 60 min of pre-irradiation are extremely different (Fig. 6b). Without pre-irradiation, the charged area is larger than in the other two cases and the charge density distribution is more spread. Also, there is no correlation between the charge density and the electron beam radial dependencies. After the pre-irradiation, the charge distribution becomes narrower and in the central part of the

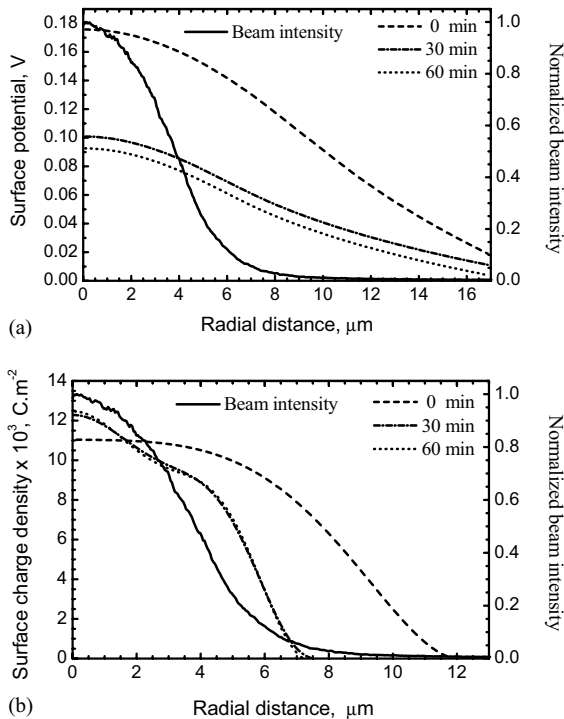


Fig. 6. Results for the reconstructed surface potential (a) and charge density (b) distributions. In each plot, the result for the three measurements (without pre-irradiation, after 30 min of pre-irradiation, and after 60 min of pre-irradiation) together with the electron beam intensity profile are plotted.

film it correlates very well with the electron beam profile.

For this complex behavior of the charge density, a simple physical explanation could be given if the dielectric permittivity is constant  $\varepsilon_r(r_k) = \varepsilon_r$  [5,8,9]. We assume that there is a uniform contamination layer residing on the film surface before the first measurement. As a rule, the intensity of the electron beam does not change significantly between the different measurements. The following three processes take place: adsorption/desorption of species on/from the film surfaces, induction of surface charge due to the irradiation, and surface charge diffusion. The diffusion of the charge due to the high mobility of the molecules in the contamination layer results in dispersed charge distribution in the first measurement. The pre-irradiation has the effect of “fixation” of the hydrocarbon molecules adsorbed on the surface. The second measurement shows localization of the charge around the beam with pronounced “bump” close to the beam edge. This bump is a result of newly adsorbed and diffusing molecules on the surface coming into the vicinity of the irradiated area and being ionized. Such ring-type contamination in the case of uniform beam intensity is described in Ref. [8].

If the experimental system is well defined, such as, uniform film without any contamination on the surface, known dielectric permittivity of the material, known electrical conductivity of the material, etc. this technique can provide much more quantitative data (e.g. absolute charge density distribution, secondary electron yield, etc.). Various parameters could be varied like beam size, beam intensity, film thickness, etc. and their effect on the above mentioned quantities observed.

## 5. Conclusion

The phase shift due to charging of amorphous carbon film (thickness 32 nm) is measured using the contrast transfer properties of the TEM. The effect of the electron bombardment on the charging is investigated by measurements after different pre-irradiation times (without pre-irradiation,

after 30 min, and 60 min). Each dataset for the phase shift is composed from two photos taken at different defocuses. The measured phase shift at a given pre-irradiation time does not depend on the defocus and no systematic error is observed in the experiments. The experimental results show that the phase shift reduces about 2 times after the first electron beam pre-irradiation. After the second pre-irradiation, significant change of the phase shift was not observed. The charging properties of the film are reaching a quasi-equilibrium state.

To obtain the radial dependence of the charge density in the film, the inverse Laplace problem for the electric potential function is solved. The appropriate boundary conditions following from the geometry of the experimental setup are used. The boundary integral method developed for step-wise charge density functions gives analytical solutions for the phase shift distribution. This approach provides numerical scheme with high efficiency for processing of the experimental data.

For each experimental dataset, the surface potential and the charge density distributions are recovered. The potential is positive and the film is positively charged. The behavior of the surface potential is similar to that of the phase shift. After 30 min of pre-irradiation, its maximum value drops from 176 to 101 mV and after that it does not change significantly. The main origin of the charging is considered to be the contamination layer on the surface of the film. The calculated distribution of the surface charge density is broader without pre-irradiation. The electron beam treatment results in a localization of the surface charge in an area slightly larger than the electron beam. The recovered distributions of the charge density after the pre-irradiation follow the measured electron beam intensity profile for small radial distances. The measurements after pre-irradiation show pronounced bump close to the beam edge.

The behavior of the charging (the localization, the bump, and the time dependence) can be explained by the contamination diffusion theory [5,8]. The quantitative investigation of these effects is a subject of future work.

## Acknowledgements

We are grateful to Dr. K. Murata for helpful discussions and H. Okawara for his help in performing the experiments. One of us (K.D.) is greatly indebted to Monbuscho international exchange program for the financial support.

## Appendix A. Calculation of the phase shift geometrical function, $f_{1,k}(r)$

If the formula for the dimensionless Fourier–Bessel image (8) is substituted into the result for the phase shift geometrical function (13), a sum of the Weber–Schafheitlin type integrals [25] is obtained. They can be evaluated in a close analytical form as

$$f_{1,k} = G_k(r, r_k) - G_k(r, r_{k-1}) - H(r), \quad (\text{A.1})$$

where the functions  $G_k$  and  $H$  are the combinations of the classical hypergeometric function  ${}_2F_1$ . The final form of the function  $H$  is

$$H(r) = \frac{r_c}{r_a} {}_2F_1\left(-\frac{1}{2}, -\frac{1}{2}; 1; \frac{r^2}{r_c^2}\right) \quad \text{for } 0 \leq r \leq r_c, \quad (\text{A.2})$$

$$H(r) = \frac{r}{r_a} {}_2F_1\left(-\frac{1}{2}, -\frac{1}{2}; 1; \frac{r_c^2}{r^2}\right) \quad \text{for } r_c \leq r \leq r_a. \quad (\text{A.3})$$

The function  $G_k$  in the interval  $0 \leq r \leq \xi$  is defined as

$$G_k(r, \xi) = -\frac{\xi^3}{3r_a(r_k^2 - r_{k-1}^2)} {}_2F_1\left(-\frac{3}{2}, \frac{1}{2}; 1; \frac{r^2}{\xi^2}\right) + \frac{\xi^3}{r_a(r_k^2 - r_{k-1}^2)} {}_2F_1\left(-\frac{1}{2}, -\frac{1}{2}; 1; \frac{r^2}{\xi^2}\right), \quad (\text{A.4})$$

and in the interval  $\xi \leq r \leq r_a$  it is

$$G_k(r, \xi) = -\frac{\xi^4}{8rr_a(r_k^2 - r_{k-1}^2)} {}_2F_1\left(\frac{1}{2}, \frac{1}{2}; 3; \frac{\xi^2}{r^2}\right) + \frac{r\xi^2}{r_a(r_k^2 - r_{k-1}^2)} {}_2F_1\left(-\frac{1}{2}, -\frac{1}{2}; 1; \frac{\xi^2}{r^2}\right). \quad (\text{A.5})$$

The convergence of the series representing the corresponding hypergeometric function is very fast and Eq. (A.1) is convenient for numerical calculations.

## References

- [1] J. Cazaux, *J. Appl. Phys.* 59 (1986) 1418.
- [2] E. Plies, in: T. Mulvey, C.J.R. Sheppard (Eds.), *Advances in Optical and Electron Microscopy*, Vol. 13, Academic Press, New York, 1994, p. 123.
- [3] J. Cazaux, *Ultramicroscopy* 60 (1995) 411.
- [4] J. Brink, M. Sherman, J. Berriman, W. Chiu, *Ultramicroscopy* 72 (1998) 41.
- [5] G. Love, V. Scott, N. Dennis, L. Laurenson, *Scanning* 4 (1981) 32.
- [6] W. Bigelow, in: A. Glauert (Ed.), *Vacuum Methods in Electron Microscopy*, Practical Methods in Electron Microscopy, Vol. 15, Portland Press, London, 1994.
- [7] L. Reimer, *Scanning Electron Microscopy. Physics of Image Formation and Microanalysis*, Springer, Berlin, 1998.
- [8] L. Reimer, *Transmission Electron Microscopy. Physics of Image Formation and Microanalysis*, Springer, Berlin, 1997.
- [9] K. Müller, *Optik* 33 (1971) 296.
- [10] P. Unwin, *Phil. Trans. R. Soc. London B* 261 (1971) 95.
- [11] K. Nagayama, *J. Phys. Soc. Jpn.* 68 (1999) 811.
- [12] R. Danev, K. Nagayama, *Ultramicroscopy* 88 (2001) 243.
- [13] G. Matteucci, G.-F. Missiroli, E. Nichelatti, A. Migliori, M. Vanzi, G. Pozzi, *J. Appl. Phys.* 69 (1991) 1835.
- [14] B. Frost, T. Jenkins, *J. Microscopy* 187 (1997) 85.
- [15] B. Frost, *Ultramicroscopy* 75 (1998) 105.
- [16] B. Frost, E. Voelkl, *Ultramicroscopy* 72 (1998) 101.
- [17] K. Danov, R. Danev, K. Nagayama, *Ultramicroscopy* 87 (2001) 45.
- [18] J. Rouse, in: T. Mulvey, C.J.R. Sheppard (Eds.), *Advances in Optical and Electron Microscopy*, Vol. 13, Academic Press, New York, 1994, p. 1.
- [19] W. Krakow, B. Siegel, *Optik* 42 (1975) 245.
- [20] T. Matsumoto, A. Tonomura, *Ultramicroscopy* 63 (1996) 5.
- [21] K. Danov, K. Nagayama, *J. Appl. Phys.*, in press.
- [22] M. Kuzuya, M. Hibino, S. Maruse, *Ultramicroscopy* 15 (1984) 233.
- [23] T. Hanai, M. Hibino, S. Maruse, *J. Electron Microsc.* 31 (1982) 360.
- [24] C. Pozrikidis, *Introduction to Theoretical and Computational Fluid Dynamics*, Oxford University Press, New York, 1997.
- [25] M. Abramowitz, I.A. Stegun (Eds.), *Handbook of Mathematical Functions with Formulas, Graphs and Mathematical Tables*, Applied Mathematics Series, Vol. 55, National Bureau of Standards, New York, 1964.